RESEARCH ARTICLE

Key Points:
- Gravity waves and ripples have been observed in winter mesopause OH* emissions at Davis Station, Antarctica, from 1999 to 2013
- Intrinsic wave propagation directions exhibited meridional anisotropy as well as seasonal and altitude-dependent zonal anisotropy
- Reverse ray tracing was used to identify the altitudinal and geographical origin of the observed waves

Correspondence to:
S. Rourke,
sharon.rourke@mu.ie

A Climatological Study of Short-Period Gravity Waves and Ripples at Davis Station, Antarctica (68°S, 78°E), During the (Austral Winter February–October) Period 1999–2013

S. Rourke[1] (ID), **F. J. Mulligan[1]**, **W. J. R. French[2]**, and **D. J. Murphy[2]** (ID)

[1]Department of Experimental Physics, National University of Ireland, Maynooth, Maynooth, Ireland, [2]Australian Antarctic Division, Kingston, Tasmania, Australia

Abstract A scanning radiometer deployed at Davis Station, Antarctica (68°S, 78°E), has been recording infrared (1.10–1.65 μm) images of a small region (24 km × 24 km) of the zenith night sky once per minute each austral winter night since February 1999. These images have been processed to extract information on the passage of gravity waves (GWs) (horizontal wavelength, $\lambda_h > 15$ km) and ripples ($\lambda_h \leq 15$ km) over the observing station. Phase speeds, periods, horizontal wavelengths, and predominant propagation directions have been deduced. Observed speeds were found to be highly correlated with horizontal wavelengths as has been reported in previous studies. Reverse ray tracing of the detected GWs only enabled us to identify four distinct groups. On average, only 15% of waves detected can be traced back to the troposphere, and a large proportion (~45%) were not successfully reverse traced substantially below the airglow layer. Two smaller groups were found to reach a termination condition for reverse ray tracing at altitudes near 50 km and 75 km. Of those that reached the termination altitude in the troposphere (10 km), most of the end points fell within a radius of 300 km of the station, with a very pronounced concentration of wave initiation to the northwest of the observing point. The predominant direction of propagation was southward, and they were observed throughout the year. Recent reports suggest the interaction of planetary waves with the background wind field as a potential source for these waves.

1. Introduction

Gravity waves (GWs) have become a subject of intense study in recent years because quantifying their influence is essential for simulations of climate change scenarios (Hamilton, 1997). Global circulation models (GCMs) employed for such simulations must include some form of parameterization scheme (Garcia et al., 2007) to represent the vertical transfer of the atmosphere's momentum and energy due to GWs since individual GWs are generally too small to be resolved by the global model grids. These parameterizations require detailed knowledge of GW characteristics such as wavelengths, phase speeds, and periods on a global scale (Alexander & Barnet, 2007). This knowledge must come from a combined set of measurements from different observation methods because, although global GW observations are available from satellites and balloons, each observation method is sensitive to only a portion of the GW spectrum and a portion of the atmosphere (Wright et al., 2016). Since GWs are intermittent in space and time, local observations are currently more accurate than global observations, with local values of momentum flux often more than an order of magnitude larger than averaged fluxes (Alexander et al., 2010). Current GCM parameterizations are not sufficient. It is already known (Choi & Chun, 2013) that GCMs do not accurately represent the intense stratospheric GW activity that occurs in the Southern Hemisphere winter. In this region, there is a known GW hot spot due to the Antarctic Peninsula and the Transantarctic Mountains (Hoffmann et al., 2013). Missing stratospheric GW drag in this region (at ~60°S) in GCMs is believed to be responsible for the so-called "cold pole problem." This is where the modeled southern polar vortex is too cold by 5–10 K, persists too long into spring, is too strong by ~10 m/s, and is located too far poleward, leading to poor predictions of ozone hole dissipation timing (Choi & Chun, 2013; McLandress et al., 2012).

Knowledge of GW activity at higher altitudes is also important. It has been long since known (Vincent & Reid, 1983) that GWs are a key driver of meridional circulation in the mesosphere from the summer to winter pole. In this paper, we study mesopause GW/ripple activity using a data set recorded from 1999 to 2013. The results
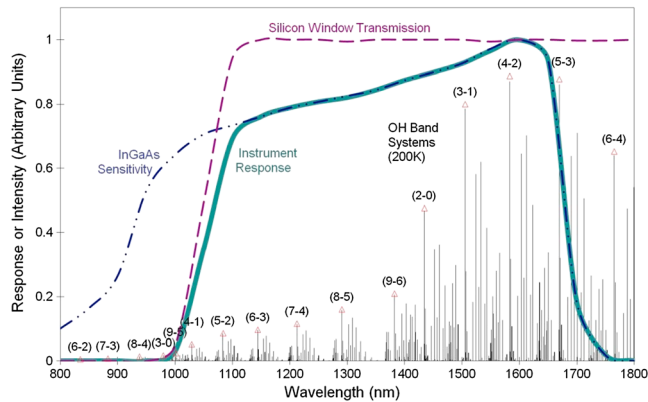
Figure 1. The emission spectrum of hydroxyl night airglow in the region of interest with typical InGaAs detector sensitivity and silicon window transmission which yield the instrument response.

of this study contribute to an international collaborative observational effort known as ANGWIN (Antarctic Gravity Wave Instrument Network) (Matsuda et al., 2017).

The Antarctic mesosphere and lower thermosphere (MLT) is recognized as one of the least understood regions of the atmosphere, and only recently has this region been investigated with a variety of different instruments (Dowdy et al., 2007). Ground-based optical studies of short-period GWs at high latitudes are particularly sparse because observation conditions are less than ideal, especially during the summer months when airglow observations cannot be made (Pautet et al., 2011). Studies on upward propagating GWs through the MLT, in the polar regions specifically, are also required for a better understanding of magnetosphere-thermosphere-ionosphere coupling, lower thermosphere dynamics, and ionospheric variabilities (Takahashi et al., 2014).

Methods of measuring GW parameters currently in use include remote sensing of temperature and wind profiles from satellites (Krebsbach & Preusse, 2007; Preusse et al., 2009), radiosondes (Leena et al., 2012; Moffat-Griffin et al., 2011; Reeder et al., 1999), rocket soundings (Goldberg et al., 2004; Rapp et al., 2001), lidar (Gardner & Voelz, 1987; Werner et al., 2007; Yang et al., 2008), radar (Hibbins et al., 2007; Vincent et al., 2010), and ground-based airglow observations (Bageston et al., 2009; Hecht et al., 2007; Nakamura et al., 1999; Nielsen et al., 2009). Part of the challenge is that GW phenomena occur over a very broad spectral range with periods ranging from minutes to several hours and spatial scales from tens to thousands of kilometers. Each observation technique tends to be sensitive only to some portion of that spectrum (Fritts & Alexander, 2003; Gardner & Taylor, 1998).

Monitoring the effects of the passage of these GWs on naturally occurring atmospheric emissions has proven to be quite an effective method of measuring their parameters (Bageston et al., 2009; Hecht et al., 2007; Nakamura et al., 1999; Nielsen et al., 2009; Yue et al., 2010). Perhaps one of the most intuitively satisfying methods is the recent class of CCD imagers currently applied to this problem (Nakamura et al., 1999; Taylor et al., 1995). In these cases, the entrance optics is frequently a fish eye lens to image almost the entire sky or a very substantial portion of it.

Hydroxyl airglow is used as a GW tracer in this study. The hydrogen-ozone reaction, $H + O_3 \rightarrow OH^*(v \leq 9) + O_2$ is the primary production mechanism for rovibrationally excited hydroxyl in the upper atmosphere (Bates & Nicolet, 1950). Production of O_3 (via $O + O_2 + M$) and loss processes through reaction with atomic oxygen and collisional quenching with O_2 and N_2 confine OH^* to a layer ~8 km thick and centered near 87 km altitude. Vibration-rotation transitions from the excited radical result in an extensive band emission spectrum ranging from ~500 nm through the near infrared region to ~4 μm, with total emission intensity ~ 5 MR (Krassovsky et al., 1962). Figure 1 shows part of this emission spectrum, with the sequence of brightest ($\Delta v = 2$ and $\Delta v = 3$) bands between 1.4 and 1.7 μm. This spectral range is covered by the instrument described in section 2.

The hydroxyl layer emission rate will respond to the propagation of GWs/ripples through the layer, both as a result of density perturbations (changing the concentration of reacting species) and temperature perturbations (changing the reaction rates) induced by the wave. Time lag and altitude differences between these mechanisms complicate the emission response, but these processes have been extensively modeled (Liu & Swenson, 2003; Makhlouf et al., 1998; Swenson & Gardner, 1998; Walterscheid et al., 1987), and generally the relative intensity perturbations are larger (by factor of ~ 8–10) than the temperature perturbations. This property is known as the Krassovsky ratio $\frac{\Delta I}{I} = \eta \left(\frac{\Delta T}{T} \right)$, where $\eta > 8$ for longer period waves (Krassovsky, 1972). Swenson and Gardner (1998) found that OH^* volume emission rate fluctuations were largest on the bottomside of the layer (~ 3 km below the OH^* peak). This was subsequently verified by satellite observations by Nikoukar et al. (2007). On the bottomside of the layer, effects due to the redistribution of atomic oxygen dominate, while fluctuations in rotational temperature are largest near the peak, thereby introducing a phase difference (greatest for short vertical wavelengths) between intensity and temperature variations. Some "filtering" of the GW spectrum (Alexander, 1998; Wright et al., 2016) is inherent in observing wave effects integrated over the OH^* layer profile. A response will only be observed if the vertical wavelength

of the GW is larger than the thickness of the layer and the period of oscillation is greater than the timescale for transport of the reacting species. As a general guide, vertical wavelengths shorter than 10 km and periods less than 10–25 min (about the chemical lifetime of O_3) (Makhlouf et al., 1998) have an attenuated response in the OH* airglow. This includes all but the shortest period GWs as the Brunt-Väisälä buoyancy period is ~ 5 min at the mesopause.

This report focuses on the analysis of a time series of "images" of the horizontal structure in OH* nightglow recorded by UWOSCR (University of Western Ontario SCanning Radiometer) in order to derive parameters of internal GWs/ripples, namely, horizontal phase velocity (v_h), direction (ϕ), wave period (T), and horizontal wavelength (λ_h). After a brief description of the instrument characteristics in section 2, the analysis method is described in section 3. Section 4 shows results obtained at Davis Station during the period 1999–2013. GW sources at Davis Station are investigated in section 5 by performing reverse ray tracing on mesopause observations. Section 6 discusses possible explanations for the asymmetry observed in the direction of GW propagation and potential sources of the GWs detected above the observing station.

2. Instrumentation

The results reported here were obtained from data (French & Mulligan, 2017) recorded by a scanning radiometer, known as UWOSCR, during the period 1999–2013. This instrument has an instantaneous field of view (FOV) of 1° and scans through a small portion of the sky (24 km×24 km) and, therefore, is most sensitive to small-scale, short-period GWs/ripples. It is one of the University of Western Ontario's near-infrared scanning radiometers, which are ground-based instruments that have been used at various locations to measure GW parameters using the hydroxyl night airglow since the early 1990s (Stockwell & Lowe, 2001a, 2001b). UWOSCR consists of a 12 cm aperture catadioptric telescope ($f/\# = 0.4$) coupled to an x-y stage, driven by stepper motors under computer control. The detector is a thermoelectrically cooled, large area planar (positive-intrinsic-negative) InGaAs photodiode which, in conjunction with the transmission cutoff of the silicon entrance window, provides a spectral response in the range 1,100 to 1,650 nm (Figure 1). This region contains some of the brightest vibration-rotation bands of OH*, primarily the (2-0), (3-1), (4-2), and (5-3) bands in the $\Delta v = 2$ sequence and the (7-4), (8-5), and (9-6) bands in the $\Delta v = 3$ sequence.

The instantaneous FOV of the telescope (1°) corresponds to a 1.5 km diameter "footprint" at the height of the airglow layer. The observing sequence drives the telescope in a raster scan of a square, 16 × 16 points in 1° increments with a dwell time per point of ~ 0.22 s, such that the 256 "pixels" in the grid are sampled in ~ 56 s. The telescope is then returned to the start position, and the sequence is repeated once per minute. The result is a 16 × 16 pixel "image" sequence with 1 min resolution, corresponding to a 24 ×24 km grid at the height of the airglow layer and centered at the zenith. Figure 2 illustrates the relationship between UWOSCR operation and the emission layer.

With the low noise and dark current of the detector, the signal-to-noise ratio of each pixel is typically ~ 100. Control software automatically starts and stops the sequence acquisition in all weather conditions between civil twilights (Sun >6° below horizon) each night. Orientation of the grid is determined by theodolite measurement of the x-y stage and by reference to stars that are clearly visible in the OH* images recorded by UWOSCR and normally occupy one pixel. Figure 3 shows an example of a sequence of 12 images (frames) from UWOSCR.

With such a small FOV, UWOSCR is most sensitive to small-scale, short-period GWs. It was believed that these waves carried momentum more efficiently and changed the velocity of the mean flow more effectively than large-scale GWs, suggesting that they were the main contributors to vertical transfer of horizontal momentum in the atmosphere (Fritts et al., 2014; Matsuda et al., 2014; Tsuda, 2014). However, a recent report by Sato et al. (2017) found that longer-period (~1 h to 1 day) waves are responsible for a larger contribution of momentum flux than short-period (~8 min to 1 h) waves in the Antarctic summer MLT. The restriction to short-period GWs in UWOSCR does have its disadvantages. For example, long-period waves are known to be less susceptible to critical-level wind filtering as they are much faster and can, therefore, propagate to higher altitudes. This makes long-period waves better suited for ray tracing studies to identify possible GW source regions (Taylor et al., 2009).
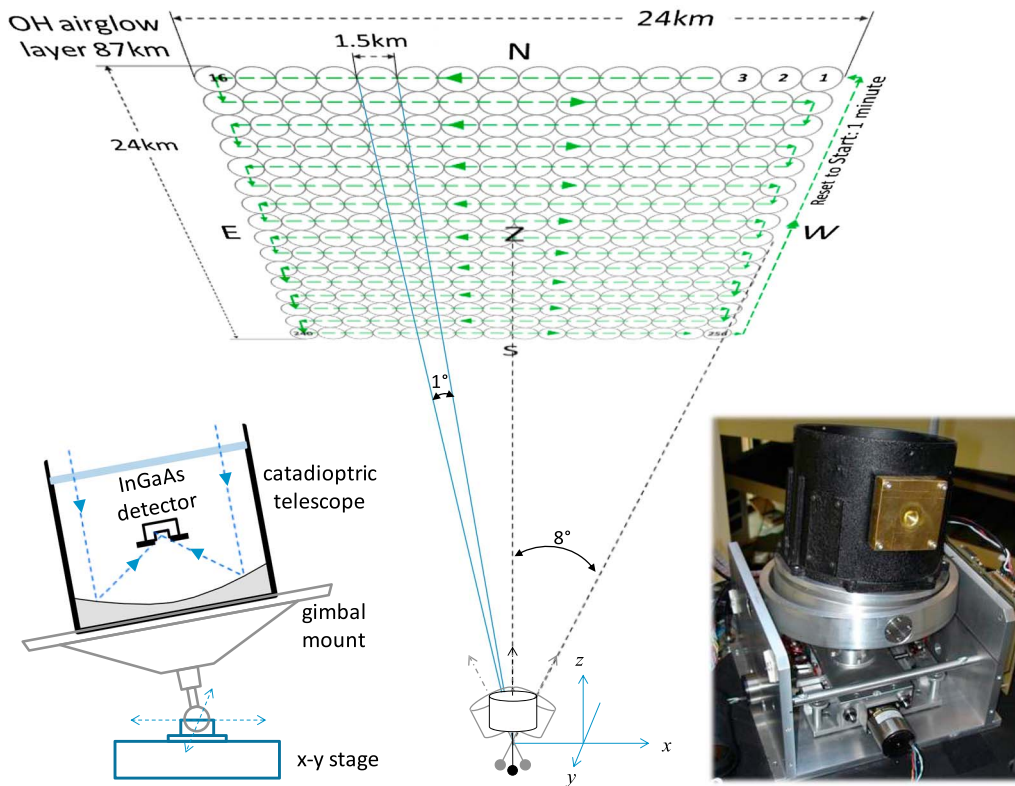
Figure 2. A schematic (left inset) of the UWOSCR instrument (right inset) and FOV at the height of the hydroxyl layer, showing the 16 × 16 point raster scan array. With a 0.22 s dwell time at each point, the field of 256 points and return to start is completed in 1 min.
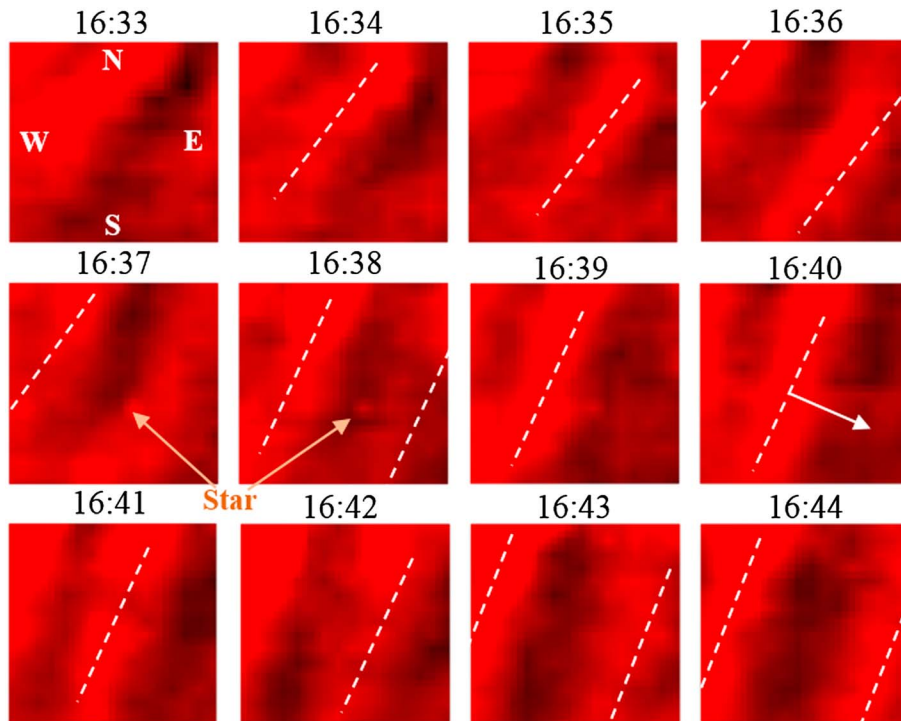

Figure 3. A sequence of 12 frames from UWOSCR on 2 July 2006 at Davis Station. The sequence shows the progression of wavefronts across the FOV (peaks indicated by dashed lines as a guide to the eye). A star is faintly visible between 16:34 and 16:39 UT.

3. Image Sequence Analysis

This section describes how the recorded image sequences are processed to determine characteristics of apparent GWs/ripples that pass through the FOV. There are quite a few techniques in use (Briggs, 1968; Coble et al., 1998; Garcia et al., 1997; Stockwell & Lowe, 2001a) that can do this. One of the main advantages of the method employed here is that it is independent of the user.

3.1. Determination of Wave Period

The period, T, of the dominant wave for a given image is determined from the fast Fourier transform (FFT) of the time variation of the weighted mean center (x_c, y_c) of 32 successive images centered on the frame in question. Weighted mean center coordinates are calculated as

$$x_c = \sum_{i=1}^{16} i \left(\sum_{j=1}^{16} s(i,j) \right) \bigg/ \sum_{i=1}^{16} \left(\sum_{j=1}^{16} s(i,j) \right) \text{and } y_c = \sum_{j=1}^{16} j \left(\sum_{i=1}^{16} s(i,j) \right) \bigg/ \sum_{j=1}^{16} \left(\sum_{i=1}^{16} s(i,j) \right)$$

where $s(i,j)$ represents the signal in a pixel with coordinates (i,j).

With a sampling rate of 1 min and a maximum window length of 32 frames, the range of wave periods detectable is 2–16 min. FFTs of sequences of both x_c and y_c are calculated separately, each providing wave amplitudes at 16 equal frequency intervals in the range from 0 to the Nyquist frequency (0.0625 min^{-1}). The peak of the frequency spectrum (maximum plus one point on either side) is fitted with a quadratic to obtain the best fit frequency. The frequency assigned to a given image is the one with the largest power. The observed period of the wave is determined from this frequency ($T = 1/f$) and can take any value in the range 2 to 16 min. As such, orographic waves are not detected by this analysis.

This method suffers from the disadvantage that it can only identify the dominant period present in the data. A series of images that contain two distinct waves with different speeds and directions will give a result that may not be a true representation of either wave.

3.2. Determination of Wave Direction and Speed

The method used to determine GW phase velocity is based on the concept of "lag analysis" or "beamsteering in the slowness domain," which is that if a wave moves across an array of sensors with little change in frequency or wave number, then the arrival times of the disturbance at each sensor can be used to calculate the wave characteristics (Briggs, 1968; Giers et al., 1997; Nappo, 2002). Two one-dimensional correlations in orthogonal directions in the image are used to determine zonal and meridional velocity components.

Cross-correlation analysis of intensity between any two pixels provides the time needed for an intensity peak to pass from one pixel to the next. The measured time lag between two pixels consists of two parts: the actual time lag between the two time series and the time lag offset between the two pixels due to the raster scan. Applying this procedure in two orthogonal directions gives the time delay for these two directions from which we can determine the direction and the phase speed (Giers et al., 1997; Nappo, 2002). Knowing the pixel separation at the nominal altitude of the OH* layer (~87 km; von Savigny et al., 2012, and references therein) to be approximately 1,500 m (angular separation of 1°), the phase speed and direction of propagation of an intensity peak can be found for the orientation of the two pixels used. Since the image contains 256 pixels, calculations are done on all possible pixel combinations at 1, 2, 3, and 4 pixel separations.

When applying the cross-correlation method to obtain the time lags, a window length must be chosen for the cross correlation. This choice depends on the persistence and the period of the waves that we hope to measure. If our choice of window length is considerably shorter than the persistence of the wave, we are not making maximum use of the available data, whereas if our window choice is longer than the persistence of the wave, our cross-correlation calculation may no longer be valid. Guided by estimates of large-amplitude waves observed in the data, the window length was set to 21 frames.

Intrinsic speed, c_i, is calculated from observed speed, c_{obs}, and coincident background wind speed in the direction of the wave, u_h, as $c_i = c_{obs} - u_h$ (Nielsen et al., 2009). Background wind was obtained from hourly averaged MF radar wind data available at 10 min intervals at an altitude of 86 km above Davis Station (Murphy & Vincent, 2000).
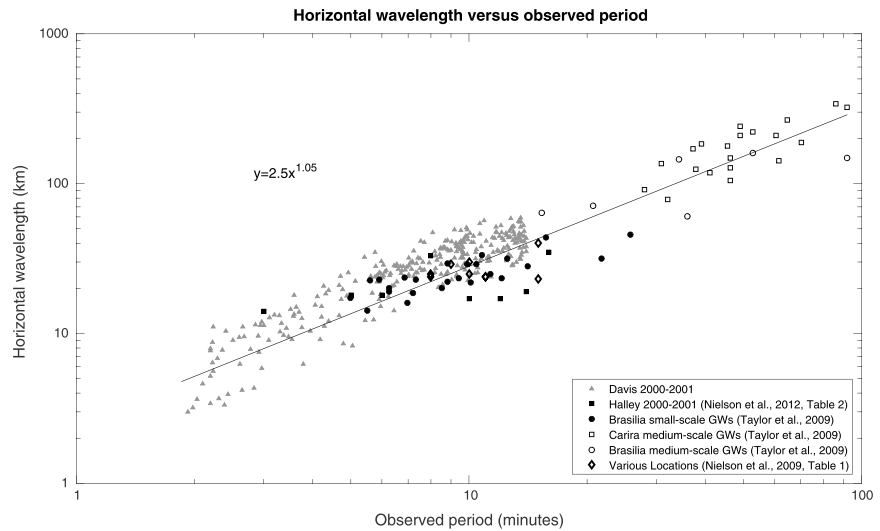
Figure 4. Comparison of the relationship between horizontal wavelength and observed period for a subset (for clarity on the plot) of Davis data with Brazil data, Halley data, and other data adapted from Taylor et al. (2009, Figure 8), Nielsen et al. (2012, Table 2), and Nielsen et al. (2009, Table 1), respectively.

The horizontal wavelength, λ_h, is calculated from $\lambda_h = c_{obs}T_{obs}$ (Lu et al., 2009), where T_{obs} is the observed period. The horizontal wavelength was also determined from the spatial lag analysis of image sequences as a check for consistency in the parameters derived.

3.3. Application of Selection Criteria

The method outlined above yields values of horizontal velocity, direction, period, and horizontal wavelength for each image recorded with the exception of 16 images at the start and end of the night. Values of these four parameters are produced by the analysis for each image, even when the UWOSCR telescope is recording detector noise only. It was necessary, therefore, to establish a robust method to eliminate false wave detections while retaining valid measurements.

The main assumption in establishing such a method is that any physical wave will be present for several minutes and that its characteristics will vary relatively slowly during that period. The assumption was implemented by applying two criteria to the variation of the velocity assigned to each image as follows. The median of the velocity was determined using a sliding five-point window centered on each image. Criterion 1 required that the velocity for a particular image be within ±7 m/s of the median. The choice of a five-point window and 7 m/s was a compromise between failing to eliminate poor data versus the risk of rejecting valid measurements. A second criterion was imposed such that results were only retained for images that satisfied criterion 1 for at least five consecutive minutes. Once again the value of five consecutive images was a compromise similar to that described earlier in this paragraph. On nights that were known to be cloudy, a few images survived the application of criterion 1, but no images survived both 1 and 2.

The sequence shown in Figure 3, of a GW passing through the FOV on 2 July 2006 between around 16:33 UT and 16:44 UT was processed as described above. The resulting wave parameters were as follows: $\phi =$ $(-24\pm3)°$ north of east, $v_h = (41 \pm 8)$ m/s, $T = (7 \pm 1)$ min, and $\lambda_h = (18 \pm 5)$ km.

4. Results

In the results presented, waves are counted such that one count corresponds to one observed wave of any duration. Figure 4 shows the results obtained from UWOSCR overlaid on results obtained from Brazil by Taylor et al. (2009); from Halley Station, Antarctica, by Nielsen et al. (2012); and from various other locations as summarized by Nielsen et al. (2009). It can be seen that all sets of results are in agreement and that the trend $\lambda_h(\text{km}) \approx 2.5(T(\text{min}))^{1.05}$ continues for even shorter periods than observed at Brazil and Halley.
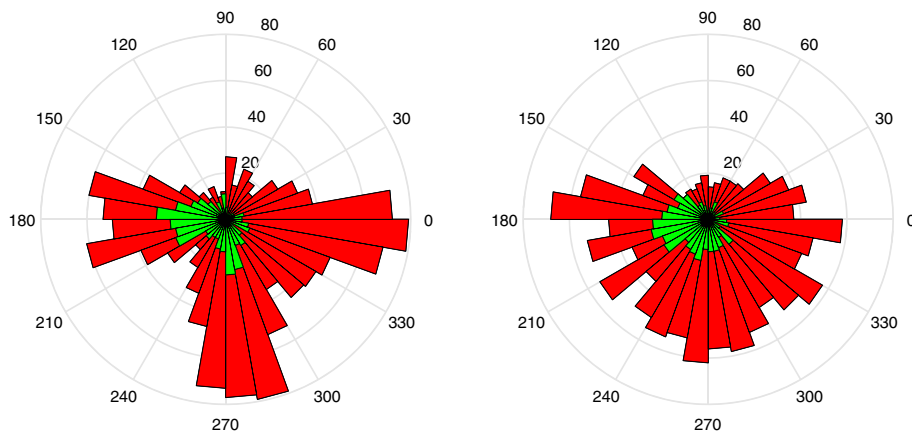
Figure 5. Histogram of (left) observed and (right) intrinsic propagation directions of bands (red) and ripples (green) above Davis Station from 1999 to 2013, where 90°=north.

From Figure 5(left), it can be seen that the observed GWs propagated in distinct directions, with the majority of band-type waves propagating poleward, westward, and eastward and the majority of ripples propagating westward and poleward. From Figure 5(right), it can be seen that there is a meridional anisotropy in intrinsic propagation directions, with very few waves propagating equatorward. However, there is no anisotropy in the zonal direction in the case of intrinsic values. A seasonal variation was also observed, where the majority of observed waves occurred in the winter months, in particular, April, May, and August, as shown in Figure 6 (bottom), and very few ripples were observed from July to October, as shown in Figure 6(top).

Figure 7 summarizes the result of our image analysis in the form of histogram plots of the observed and intrinsic wave characteristics during the period 1999–2013. Figure 7a shows that there are two distinct distributions for horizontal wavelengths, one for ripples (where typically $\lambda_h \approx 8$–10 km) and one for bands (where typically $\lambda_h \approx 24$–26 km). From Figure 7b it can be seen that waves typically persist for ~6–8 min, but, in rare cases, waves persist for up to ~20–70 min. Figure 7c shows a more symmetric distribution of observed phase speeds with ripples usually propagating at observed horizontal phase speeds of ~40–60 m/s and bands usually propagating with speeds of ~50–80 m/s. From Figure 7d, it can be seen that the observed period of ripples is usually between 2 and 3 min (reminiscent of remnant turbulent structures; Hecht et al., 2014) and the observed period of bands appear to have two maxima at ~7 min and ~13 min, although the latter may partially be an artifact of the analysis as there is an artificial upper boundary at 16 min. Figures 7e and 7f show the corresponding intrinsic values to Figures 7c and 7d, respectively. It is noted that the intrinsic speed of ripples is not calculated to be 0 (Figure 7e) suggesting that their position changes independently of the background wind.

5. Ray Tracing

In an effort to understand our observations, we performed reverse ray tracing of the GWs observed above Davis Station using the approach described by Marks and Eckermann (1995) and implemented by Wrasse et al. (2006) and Tateno and Sato (2008) and more recently in Pramitha et al. (2015). Although the intrinsic speed of the ripples is not calculated to be 0 (Figure 7e), they have been excluded from the ray tracing because some of these may result from turbulence and instabilities (e.g., Hecht et al., 2014). In such cases, their inclusion in the ray tracing could invalidate the resultant statistics. Ideally, detailed knowledge of the wind and temperature fields within a radius of about 500 km above the observing station would be available for the reverse ray tracing. Such data are rare, with the result that climatological models of wind and temperature are usually employed as the best available substitute. The background wind used here for reverse ray tracing was obtained from the Horizontal Wind Model (HWM-07) (Drob et al., 2008), while the temperature data were taken from the MSIS-E-90 model (Hedin, 1991). A "cube" of wind and temperature data (Eckermann & Marks, 1997) 10° in latitude, 30° in longitude, and in the altitude range 0–100 km was created centered on Davis Station for each day of the year. The grid spacing within the segment was 1° latitude, 3° longitude, and 1 km in the vertical direction. Cubic spline interpolations were used in all
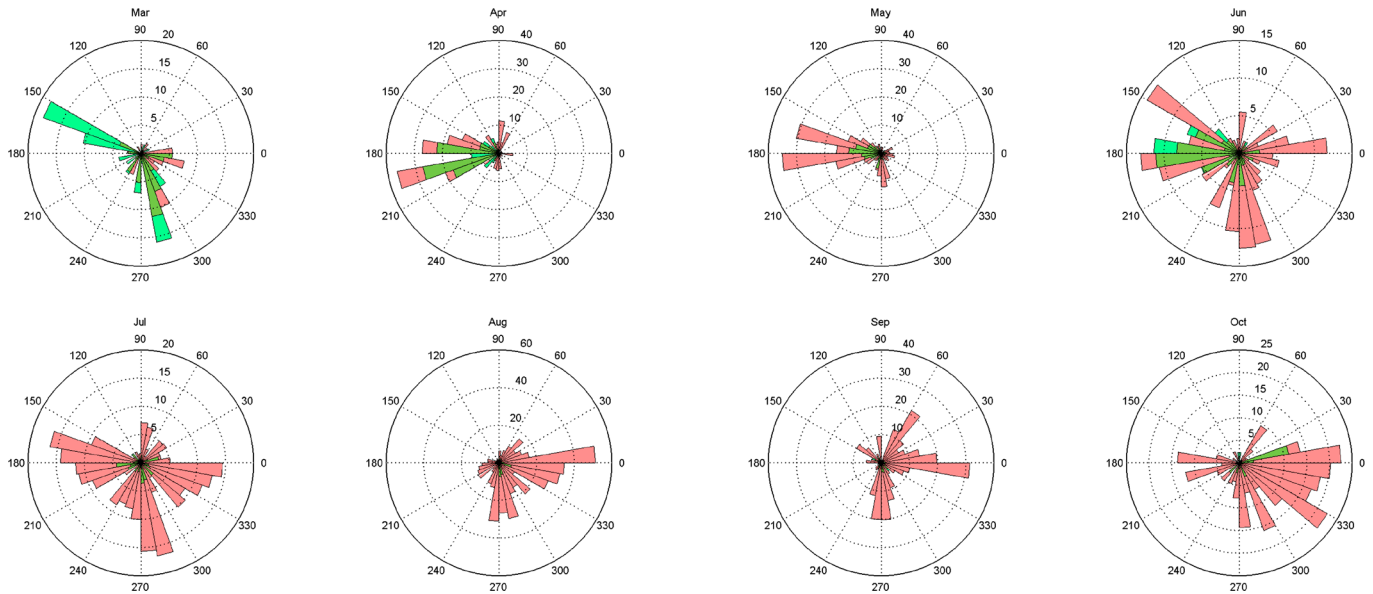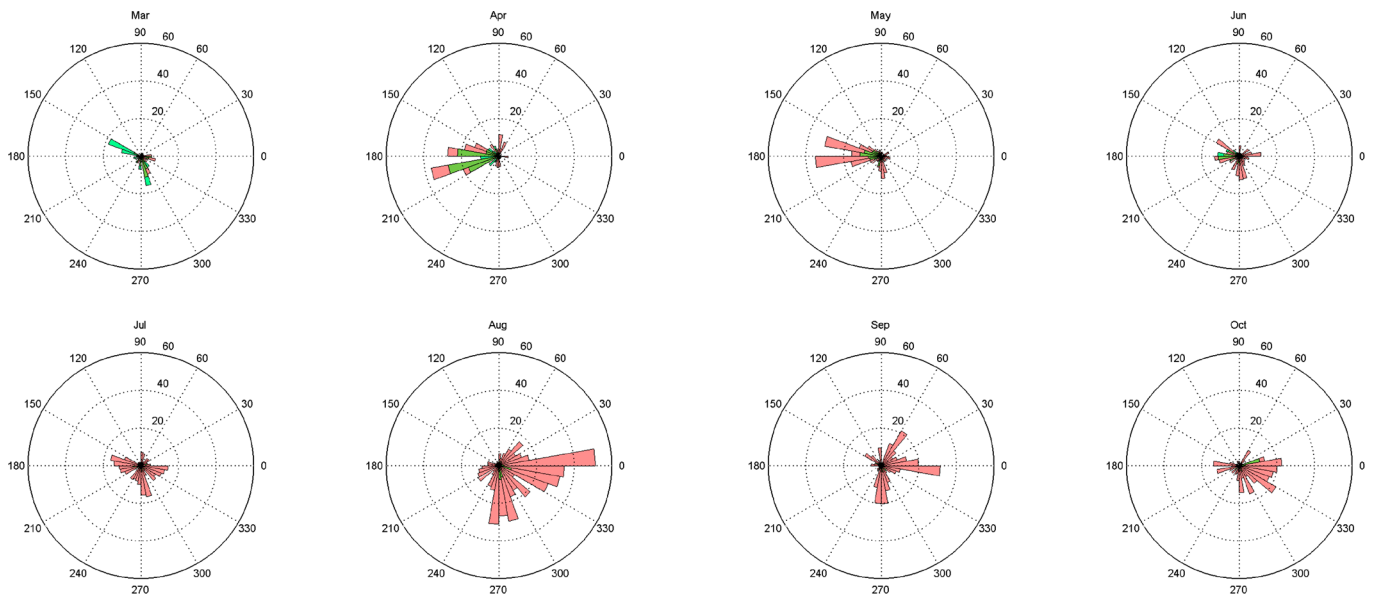
Figure 6. Distribution of observed GW (red) and ripple (green) propagation directions, organized by month. Counts are given as the time in which wave events were detected as a percentage of the total observing time in that particular month, scaled up by a factor of 500. Distributions are presented with both (top) an autoscaled and (bottom) a fixed radial axis, with maximum percentage = 60%. The total number of minutes during which waves were detected in August (all years) was 3,584.

three dimensions to ensure that the spatial derivatives of the background atmospheric parameters varied smoothly to satisfy the WKB (Wentzel-Krammers-Brillouin) approximation used in deriving the ray tracing equations (Eckermann & Marks, 1997). Interpretation of the ray tracing results below must be tempered with the knowledge that the actual wind and temperature field may differ significantly from the climatological values used.

Each GW detected by the UWOSCR instrument was specified by an intrinsic wave phase speed, intrinsic propagation direction, horizontal wavelength, and intrinsic period at the mean altitude of the OH* emission layer (~87 km). Intrinsic parameters were obtained using the locally measured radar winds at the hour of observation. The wave was then reverse ray traced until it reached the troposphere termination altitude
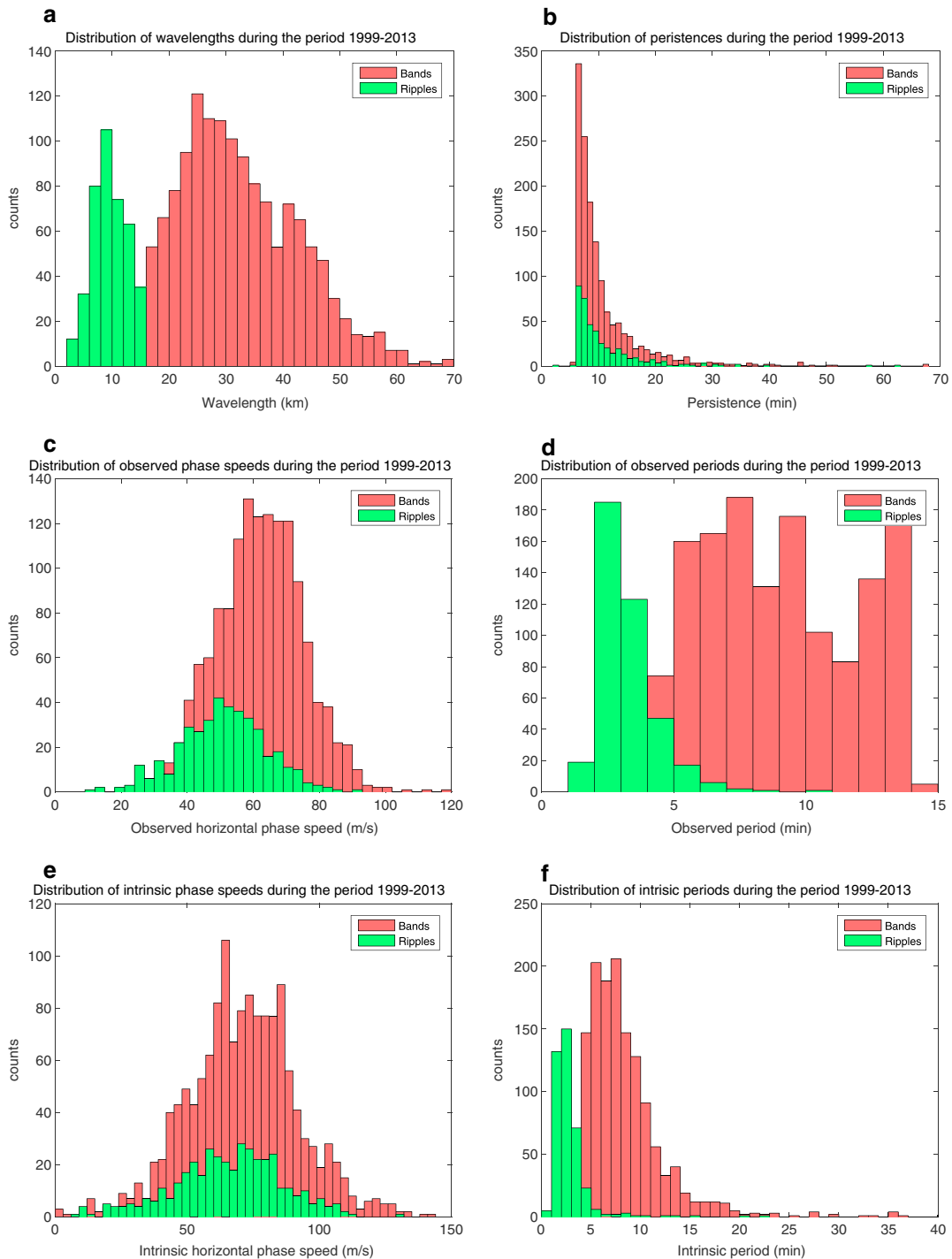
Figure 7. Histograms of (a) horizontal wavelengths, (b) persistence, (c) observed horizontal phase speeds, (d) observed periods, (e) intrinsic horizontal phase speeds, and (f) intrinsic periods for all GWs observed during the period 1999–2013.

(10 km) or until the conditions for wave propagation were no longer valid. Following Wrasse et al. (2006) and Pramitha et al. (2015), the four conditions applied when wave propagation is no longer valid were (1) the WKB approximation used to derive the ray tracing equations no longer holds; (2) the vertical wave number squared, $m^2 < 0$, which means that the wave cannot propagate vertically; (3) the intrinsic frequency $\hat{\omega} < 0$ or close to 0 meaning that the wave is approaching a critical layer; and (4) $m^2 > 1 \times 10^{-6}$ (cycles^2/m^2), which means that the vertical wavelength becomes smaller than 1 km and close to a critical level. In
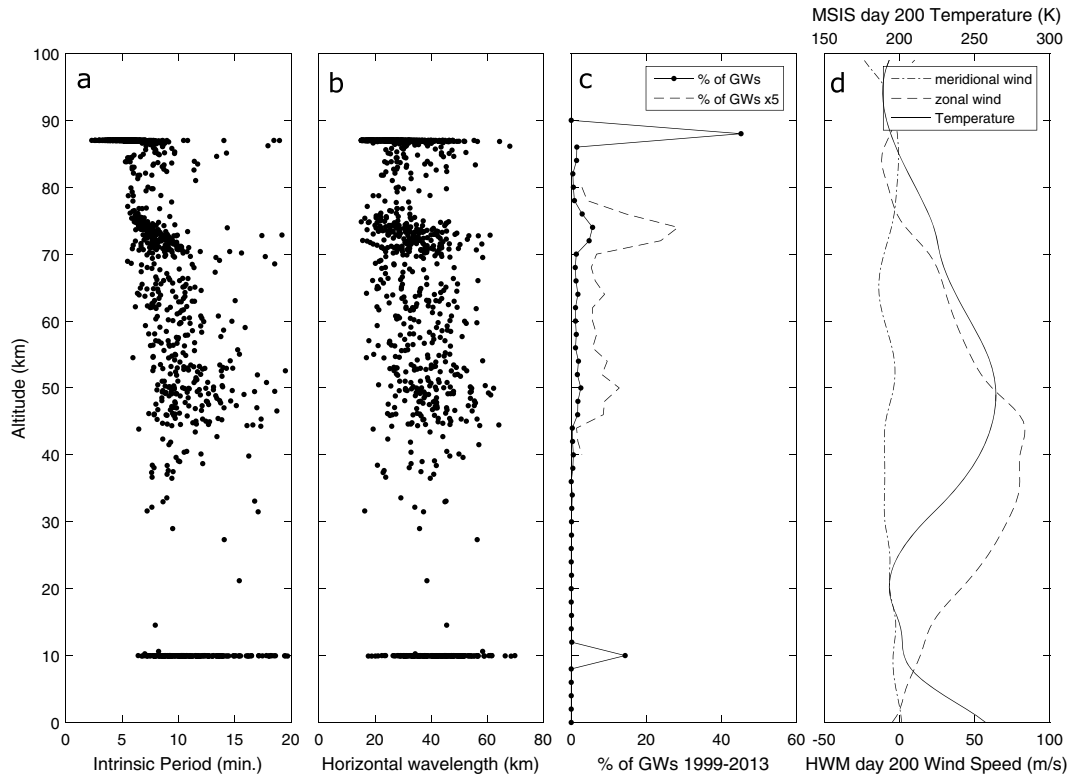
Figure 8. Termination altitude of traced GWs as a function of (a) period, (b) horizontal wavelength, and (c) number of traced GWs. (d) Typical wintertime (day of year = 200) wind and temperature profiles at Davis Station, obtained from HWM-07 and MSIS-E-90 models, respectively.

practice, condition (4) always occurred before condition (3) was reached. A total of 1,407 individual waves over the period 1999 to 2013 were reverse ray traced using this method. Typical uncertainties in the reverse ray tracing results arising from uncertainties in the wave parameter measurements are approximately 1° longitude, 0.25° latitude, and 5 km altitude, although the uncertainty on altitude is very dependent on the terminating point.

A summary of the results of the reverse ray tracing is illustrated in Figure 8c, which shows the percentage of waves that reached a given altitude before a termination condition occurred. On average, ~15% of the GWs detected at the altitude of the OH* layer near the mesopause reached the troposphere termination at 10 km. This is consistent with reports from Wrasse et al. (2006) and Kim et al. (2010) who found that 15% (at Cachoeira Paulista, Brazil) and 23% (at Mount Bohyun, Korea) respectively of waves were traceable to the troposphere, while more than 70% were of mesospheric origin. A large proportion (45%) of the waves ray traced reached the termination condition at, or only slightly below, the altitude of detection (~87 km) because $m^2 < 0$, which means that the atmospheric conditions were unfavorable for vertical wave propagation. This may imply a large proportion of ducted waves that are trapped near the airglow layer.

The altitude profile of the traced waves shows two small but well-defined peaks, one near 50 km and the other at 74 km. The peak near 50 km appears to correspond to the middle atmospheric jet. The termination condition for the majority of those in the peak near 50 km was $m^2 > 1 \times 10^{-6}$ (cycles^2/m^2), which means that the vertical wavelength was smaller than 1 km and close to a critical level. The group of waves with termination points between 70 and 80 km tend to have intrinsic periods in the range 7–9 min and horizontal wavelengths in the range 26–38 km (see Figure 8), whereas the group of waves with termination points between 45 and 55 km tend to have longer intrinsic periods (9–13 min) and horizontal wavelengths (34–46 km).

Figure 9 shows the percentage of waves that reach the troposphere for each year. The GWs that reach the troposphere in the reverse ray tracing are characterized by having (1) directions that are predominantly southward, (2) λ_h generally between ~35 and 48 km, and (3) intrinsic periods > ~6.5 min. In contrast, the waves for which the reverse ray tracing terminates near the detection altitude (~87 km) have intrinsic
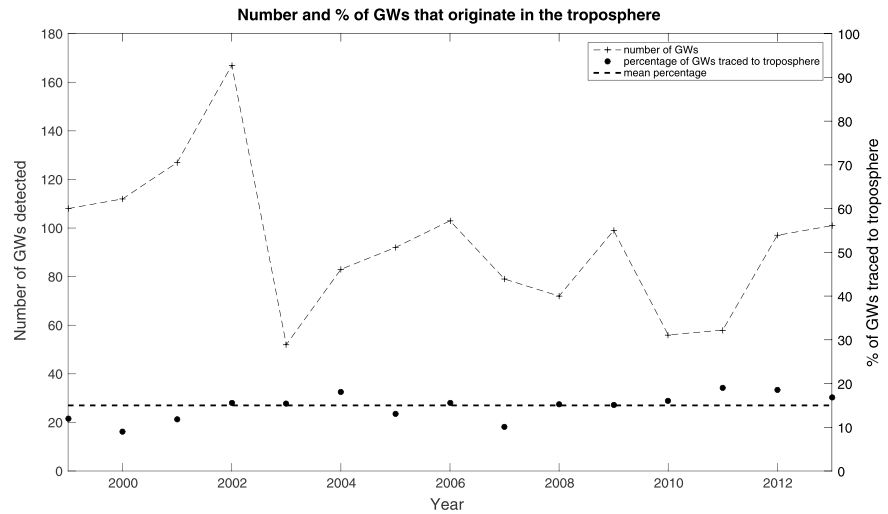
Figure 9. Number of waves detected by year (crosses) and percentage of those waves traced to troposphere (dots). The dashed black horizontal line is the mean percent of waves traced to the troposphere over all years.

periods generally between ~4.5 and 6.5 min and horizontal wavelengths that are generally between 20 and 30 km.

The geographic location of the wave end points that reached the termination altitude (10 km) in the troposphere (204 waves), the 45–55 km region (134 waves), and the 70–80 km region (208 waves) are shown in Figure 10 with the majority of the points falling within a radius of 300 km of the station. These results are discussed in section 6.

Figure 11 shows histograms of the seasonal variation and direction of propagation of the three groups of waves identified by the vertical profile in the reverse ray tracing. The tropospheric group (Figure 11, bottom
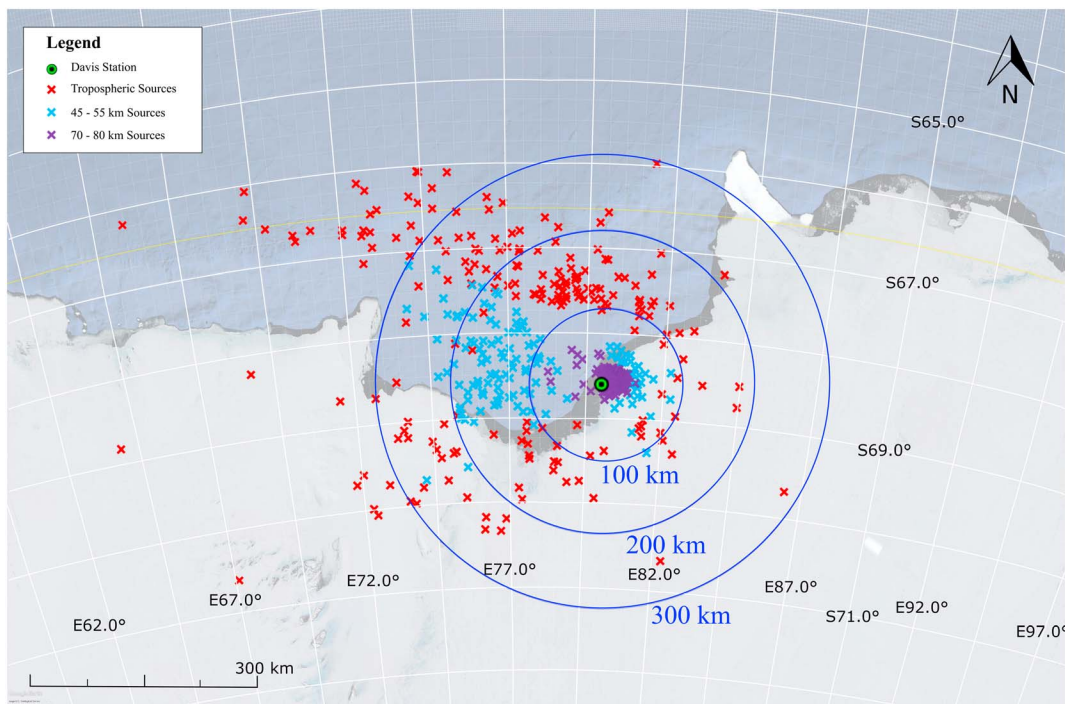

Figure 10. Geographic distribution of the end points of GWs with termination points reverse ray traced to the troposphere (red), the 45–55 km altitude region (blue), and the 70–80 km altitude region (purple).
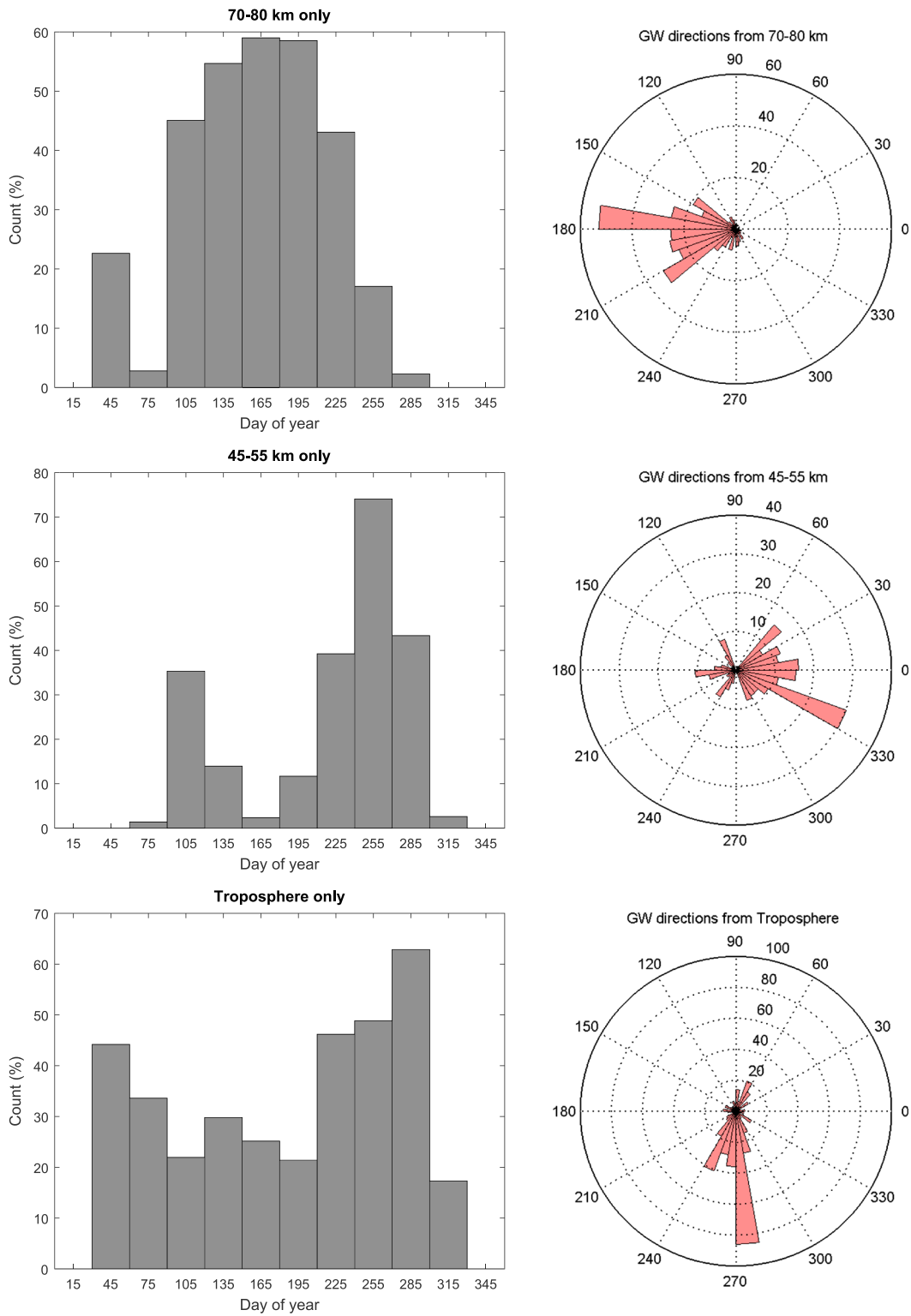
Figure 11. Seasonal and directional distribution of the GWs for three populations selected according to the altitude that the reverse ray tracing terminated. The groups terminated (bottom row) in the troposphere, (middle row) at an altitude range 45–55 km, and (top row) at an altitude range 70–80 km. Counts are given as the time in which wave events were detected as a percentage of the total observing time in that particular month, scaled up by a factor of 500.

row) have a very pronounced southward direction of propagation, with a large peak during August–October and minor peaks in February and in May.

The group with ray traced end points at 45–55 km (Figure 11, middle row) have a maximum in the early austral spring period (September) with a smaller peak in late autumn (April). The September group propagate predominantly eastward, whereas the April group tend to be westward propagating. The group that terminate ray tracing in the 70–80 km altitude region (Figure 11, top row) show a strong midwinter maximum and are generally directed westward. The quite different directions of the three groups and the seasonal difference in their occurrence is discussed in greater detail in section 6.

6. Discussion

Ground-based airglow observations made during February–October over 15 years at Davis Station are used to construct a climatology of the horizontal characteristics of GWs and ripples near the mesopause. The main findings are

1. Two distinct distributions of horizontal wavelength were observed (as shown in Figure 7), both obeying the relation $\lambda_h(\text{km}) \approx 2.5T(\text{min.})^{1.05}$. This trend is consistent with previous results (Nielsen et al., 2009, 2012; Taylor et al., 2009), as shown in Figure 4, but is now extended to include shorter horizontal wavelengths.
2. An unusual distribution of propagation directions over Davis Station was observed, as shown in Figure 5. There was a difference in the observed directional distribution of GWs and ripples, and so they were considered separately. A clear preference for poleward, eastward, and westward propagating GWs was observed but with few ripples propagating eastward. There was also a lack of equatorward waves, a result that is generally consistent with previous high-latitude studies (Matsuda et al., 2014; Nielsen et al., 2009; Suzuki et al., 2009). When the intrinsic directions of the GWs and ripples were determined (by taking account of the background wind from the coincident MF radar wind measurements), the "gaps" in the non-Cartesian directions disappeared as shown in Figure 5(right). Propagation directions will be discussed in further detail below.
3. Ray tracing enabled us to identify four distinct groups among the full set of GWs, each group classified by their termination altitudes as follows: waves that reached a termination condition at ~87 km altitude (~45% of total number of observed waves), those that terminate between 70 and 80 km (~15% of total number of observed waves), those that terminate between 45 and 55 km altitude (~9.5% of total number of observed waves), and finally those that terminate in the troposphere (~15% of total number of observed waves). These groups can be seen in Figures 8a–8c.
4. The timing of GW/ripple activity during the period March–October can be seen in Figure 6 (bottom). The majority of waves observed were in the winter months, with peaks in April, May, and August. This is in good agreement with Dowdy et al. (2007), who studied the seasonal variation of GWs with periods ranging from 20 to 120 min above Davis Station between 1994 and 2005 using MF radar. They found a peak of GW activity during the winter months, with two smaller peaks in March and August.

We consider two possible explanations for the seasonal variability and prominent distribution of GW propagation directions observed: source variability and vertical critical-level filtering, which has been extended to include turning level reflection (Tomikawa, 2015), in the stratospheric mean wind. We first consider vertical critical-level filtering (linking the springtime breakdown of the polar vortex to mesospheric GWs). During the winter, a very strong eastward circulation develops in the polar stratosphere, usually reaching wind speeds of more than ~80 m/s (HWM-07). This jet can block eastward propagating waves (Matsuda et al., 2014; Tomikawa, 2015; Tsuda, 2014), except those whose phase speeds are larger than the eastward wind speed, from moving upward past the stratosphere, while westward propagating waves can move freely upward.

Since ripples have shorter wavelengths than GWs as shown in Figure 7a, they are considerably more susceptible to both critical-level filtering and particularly to turning level reflection, because their periods become shorter than the Brunt-Väisälä period in the large vertical shear as explained by Tomikawa (2015). This could explain why ripples would be almost all filtered out, and, as a result, there would be many fewer ripples than GWs observed in the winter mesopause (as is the case above Davis). When the polar vortex breaks down in springtime, the zonal wind reverses, facilitating eastward propagating GWs while blocking westward

propagating GWs (Kaifler et al., 2015). This is consistent with our climatological observations shown in Figure 6 where there is a strong westward lobe in May and a strong eastward lobe in August. It is also in agreement with Alexander et al. (2011), who studied GWs in the upper stratosphere and lower mesosphere (USLM) region above Davis Station during the winters of 2007–2008 and found that GWs dissipate above ~40 km, where the zonal wind speed is at its maximum. However, based on our ray tracing results, the eastward propagating waves observed do not have tropospheric sources—they belong to the 45–55 km source region (as shown in Figure 11, right column), which is above the polar jet. Based on this, we reject critical-level filtering as an explanation for the distinct seasonal dependent zonal anisotropy in our observed GW directions.

The second explanation that we consider for the distinct seasonal dependent zonal anisotropy in GW directions observed is GW sources around Davis Station and their variability. Initial qualitative assessments about GW source regions can be obtained from Figure 5. First, the lack of waves propagating northward above Davis Station and the absence of a significant meridional wind bias (Figure 8d) suggests that the region poleward of Davis Station is a weak GW source. In particular, the prominent GW propagation directions indicate that possible candidate sources of observed GWs are to the north (over the Davis Sea or Indian Ocean), to the west (toward the Amery Ice Shelf), or to the east (toward the Vestfold Hills and the West Ice Shelf). Based on our ray tracing results, four main altitude source regions have been identified. The group that could not be ray traced significantly below the observing altitude generally have periods of ~4.5–6.5 min and horizontal wavelengths of ~20–30 km, and they have a broad spread of propagation directions but with a notable absence of northward headings. Each of the other three groups exhibited a particular propagation direction preference, as shown in Figure 11(right column).

The geographic location of the wave end points that reached each of these altitude regions is shown in Figure 10. It was found that almost all the waves that were traced to between 70 and 80 km (208 waves) occurred in midwinter (June and July), were locally generated to the east of the station, and were propagating westward at the detection altitude. Most of the waves that were traced to just above the stratospheric jet, between 45 and 55 km (134 waves), were generated either to the east or west of the station and were propagating either eastward or westward at the detection altitude. Most of these waves occurred in May and August, which corresponds to the timing of the formation and breakdown of the polar vortex. The waves that were traced all the way down to the troposphere (204 waves) have intrinsic periods greater than 6.5 min, horizontal wavelengths greater than 20 km, and propagation directions predominantly southward; show a very pronounced concentration of wave initiation to the northwest at approximately 100–300 km from the observing point; and occurred consistently throughout all seasons. One possibility for the origin of these waves is the interaction of planetary waves with the background wind fields, as discussed recently by Mehta et al. (2017) for the case of short-period mesospheric GWs detected at the South Pole. A detailed investigation of this hypothesis for the waves reported here is beyond the scope of this work.

In terms of tropospheric sources, Alexander and Murphy (2015) reported that GW production in the lower troposphere above Davis Station was at its most active when large-scale low-pressure systems produced southwestward wind flow that enhanced katabatic winds over the station. The principal source of these GWs was believed to be airflow over an ice ridge line approximately 60 km northeast of Davis, oriented at ~90° with respect to the wind. However, these GWs (orographic in origin) were not expected to reach the middle atmosphere because of low-level (midtroposphere) critical filtering (Alexander & Murphy, 2015). This latter point is supported by our ray tracing results in which virtually no waves reached the troposphere in this geographical region.

Alexander et al. (2011) suggested that GW variability in the USLM above Davis Station may be due to a large source variability or in situ GW generation by the polar vortex, and they ruled out Doppler shifting by background winds in the region. The seasonal variation and propagation direction of the GWs with end points in this region (45–55 km) based on our ray tracing results is consistent with their generation by the polar vortex. This is also in agreement with Sato et al. (2009, Figure 3), who identified Antarctic regions that have a high GW momentum flux in the winter lower stratosphere. From their map, it can be seen that Davis has a momentum flux with an absolute value of 2–4 mPa, most likely indicating either a topographical source in the region or spontaneous GW emission from the strong eastward jets and fronts (Sato et al., 2009).

7. Conclusions

In this paper, we process and analyze ground-based OH* airglow images from Davis Station dating from 1999 to 2013 (excluding summer months) to extract information about the horizontal structure of GWs ($\lambda_h >$ 15 km) and ripples ($\lambda_h \leq$ 15 km) at ~87 km altitude. A climatology of phase speeds, horizontal wavelengths, periods, and propagation directions is presented.

Horizontal wavelengths and periods were found to be highly correlated, such that $\lambda_h(km) \approx 2.5T(min)^{1.05}$, as has been found in previous studies. Source altitude and seasonal dependent predominant propagation directions were observed. Most waves were observed to occur during April, May, and August, which approximately corresponds to the beginning and end of the polar vortex. The predominant wave directions over the station is southward, eastward, and westward for GWs and southward and westward for ripples. We suggest that source variability may be a contributing factor in why we observe these pronounced directions, but further investigation is required to determine the exact cause.

References

Alexander, M. J. (1998). Interpretations of observed climatological patterns in stratospheric gravity wave variance. *Journal of Geophysical Research*, *103*(D8), 8627–8640. https://doi.org/10.1029/97JD03325

Alexander, M. J., & Barnet, C. (2007). Using satellite observations to constrain parameterizations of gravity wave effects for global models. *Journal of the Atmospheric Sciences*, *64*(5), 1652–1665. https://doi.org/10.1175/JAS3897.1

Alexander, M. J., Geller, M., McLandress, C., Polavarapu, S., Preusse, P., Sassi, F., … Watanabe, S. (2010). Recent developments in gravity-wave effects in climate models and the global distribution of gravity-wave momentum flux from observations and models. *Quarterly Journal of the Royal Meteorological Society*, *136*(650), 1103–1124. https://doi.org/10.1002/qj.637

Alexander, S. P., Klekociuk, A. R., & Murphy, D. J. (2011). Rayleigh lidar observations of gravity wave activity in the winter upper stratosphere and lower mesosphere above Davis, Antarctica (69°S, 78°E). *Journal of Geophysical Research*, *116*, D13109. https://doi.org/10.1029/2010JD015164

Alexander, S. P., & Murphy, D. (2015). The seasonal cycle of lower-tropospheric gravity wave activity at Davis, Antarctica (69°S, 78°E). *Journal of the Atmospheric Sciences*, *72*(3), 1010–1021. https://doi.org/10.1175/JAS-D-14-0171.1

Bageston, J. V., Wrasse, C. M., Gobbi, D., Takahashi, H., & Souza, P. B. (2009). Observation of mesospheric gravity waves at Commandante Ferraz Antarctic Station (62°S). *Annales de Geophysique*, *27*(6), 2593–2598. https://doi.org/10.5194/angeo-27-2593-2009

Bates, D. R., & Nicolet, M. (1950). The photochemistry of atmospheric water vapor. *Journal of Geophysical Research*, *55*(3), 301–327. https://doi.org/10.1029/JZ055i003p00301

Briggs, B. H. (1968). On the analysis of moving patterns in geophysics—I. Correlation analysis. *Journal of Atmospheric and Terrestrial Physics*, *30*(10), 1789–1794. https://doi.org/10.1016/0021-9169(68)90098-6

Choi, H. J., & Chun, H. Y. (2013). Effects of convective gravity wave drag in the Southern Hemisphere winter stratosphere. *Journal of the Atmospheric Sciences*, *70*(7), 2120–2136. https://doi.org/10.1175/JAS-D-12-0238.1

Coble, M., Papen, G. C., & Gardner, C. S. (1998). Computing two-dimensional unambiguous horizontal wavenumber spectra from OH airglow images. *IEEE Transactions on Geoscience and Remote Sensing*, *36*(2), 368–382. https://doi.org/10.1109/36.662723

Dowdy, A. J., Vincent, R. A., Tsutsumi, M., Igarashi, K., Murayama, Y., Singer, W., & Murphy, D. J. (2007). Polar mesosphere and lower thermosphere dynamics: 1. Mean wind and gravity wave climatologies. *Journal of Geophysical Research*, *112*, D17104. https://doi.org/10.1029/2006JD008126

Drob, D. P., Emmert, J. T., Crowley, G., Picone, J. M., Shepherd, G. G., Skinner, W., … Vincent, R. A. (2008). An empirical model of the Earth's horizontal wind fields: HWM07. *Journal of Geophysical Research*, *113*, A12304. https://doi.org/10.1029/2008JA013668

Eckermann, S. D., & Marks, C. J. (1997). GROGRAT: A new model of the global propagation and dissipation of atmospheric gravity waves. *Advances in Space Research*, *20*(6), 1253–1256. https://doi.org/10.1016/S0273-1177(97)00780-1

French, W. J. R., & Mulligan, F. J. (2017). Scanning radiometer observations of hydroxyl airglow over Davis, Antarctica, 1999–2016, Aust. Antarct. Data Cent. - CAASM Metadata, https://doi.org/10.4225/15/59114b64b057f. Retrieved from https://data.aad.gov.au/metadata/records/AAS_4157_Davis_UWOSCR_1999-2016

Fritts, D. C., & Alexander, M. J. (2003). Gravity wave dynamics and effects in the middle atmosphere. *Reviews of Geophysics*, *41*(1), 1003. https://doi.org/10.1029/2001RG000106

Fritts, D. C., Pautet, P. D., Bossert, K., Taylor, M. J., Williams, B. P., Iimura, H., … Stober, G. (2014). Quantifying gravity wave momentum fluxes with mesosphere temperature mappers and correlative instrumentation. *Journal of Geophysical Research: Atmospheres*, *119*, 13,583–13,603. https://doi.org/10.1002/2014JD022150

Garcia, F. J., Taylor, M. J., & Kelley, M. C. (1997). Two-dimensional spectral analysis of mesospheric airglow image data. *Applied Optics*, *36*(29), 7374–7385. https://doi.org/10.1364/AO.36.007374

Garcia, R. R., Marsh, D. R., Kinnison, D. E., Boville, B. A., & Sassi, F. (2007). Simulation of secular trends in the middle atmosphere, 1950–2003. *Journal of Geophysical Research*, *112*, D09301. https://doi.org/10.1029/2006JD007485

Gardner, C. S., & Taylor, M. J. (1998). Observational limits for lidar, radar, and airglow imager measurements of gravity wave parameters. *Journal of Geophysical Research*, *103*(D6), 6427–6437. https://doi.org/10.1029/97JD03378

Gardner, C. S., & Voelz, D. G. (1987). Lidar studies of the nighttime sodium layer over Urbana, Illinois: 2. Gravity waves. *Journal of Geophysical Research*, *92*(A5), 4673–4974. https://doi.org/10.1029/JA092iA05p04673

Giers, D. H., Sahai, Y., Cogger, L. L., & Ryan, E. H. (1997). Occurrence characteristics of mesospheric gravity waves at 51°N. *Journal of Atmospheric and Solar - Terrestrial Physics*, *59*(10), 1197–1203. https://doi.org/10.1016/S1364-6826(96)00117-4

Goldberg, R. A., Fritts, D. C., Williams, B. P., Lübken, F.-J., Rapp, M., Singer, W., … Krueger, D. A. (2004). The MaCWAVE/MIDAS rocket and ground-based measurements of polar summer dynamics: Overview and mean state structure. *Geophysical Research Letters*, *31*, L24S02. https://doi.org/10.1029/2004GL019411

Hamilton, K. (Ed.) (1997). *Gravity wave processes: Their parameterization in global climate models, NATO ASI Series: Global Environmental Change* (Vol. 50). Berlin: Springer. https://doi.org/10.1007/978-3-642-60654-0

Hecht, J. H., Liu, A. Z., Walterscheid, R. L., Franke, S. J., Rudy, R. J., Taylor, M. J., & Pautet, P. D. (2007). Characteristics of short-period wavelike features near 87 km altitude from airglow and lidar observations over Maui. *Journal of Geophysical Research*, *112*, D16101. https://doi.org/10.1029/2006JD008148

Hecht, J. H., Wan, K., Gelinas, L. J., Fritts, D. C., Walterscheid, R. L., Rudy, R. J., … Swenson, G. R. (2014). The life cycle of instability features measured from the Andes Lidar Observatory over Cerro Pachon on 24 March 2012. *Journal of Geophysical Research: Atmospheres*, *119*, 8872–8898. https://doi.org/10.1002/2014JD021726

Hedin, A. E. (1991). Extension of the MSIS thermosphere model into the middle and lower atmosphere. *Journal of Geophysical Research*, *96*(A2), 1159–1172. https://doi.org/10.1029/90JA02125

Hibbins, R. E., Espy, P. J., Jarvis, M. J., Riggin, D. M., & Fritts, D. C. (2007). A climatology of tides and gravity wave variance in the MLT above Rothera, Antarctica obtained by MF radar. *Journal of Atmospheric and Solar - Terrestrial Physics*, *69*(4-5), 578–588. https://doi.org/10.1016/j.jastp.2006.10.009

Hoffmann, L., Xue, X., & Alexander, M. J. (2013). A global view of stratospheric gravity wave hotspots located with Atmospheric Infrared Sounder observations. *Journal of Geophysical Research: Atmospheres*, *118*, 416–434. https://doi.org/10.1029/2012JD018658

Kaifler, B., Lübken, F.-J., Höffner, J., Morris, R. J., & Viehl, T. P. (2015). Lidar observations of gravity wave activity in the middle atmosphere over Davis (69°S, 78°E), Antarctica. *Journal of Geophysical Research: Atmospheres*, *120*, 4506–4521. https://doi.org/10.1002/2014JD022879

Kim, Y. H., Lee, C. S., Chung, J. K., Kim, J. H., & Chun, H. Y. (2010). Seasonal variations of mesospheric gravity waves observed with an airglow all-sky camera at Mt. Bohyun, Korea (36°N). *The Journal of Astronomy Space Science*, *27*(3), 181–188. https://doi.org/10.5140/JASS.2010.27.3.181

Krassovsky, V. I. (1972). Infrasonic variations of OH emission in the upper atmosphere. *Annales de Geophysique*, *77*(4), 254–259.

Krassovsky, V. I., Shefov, N. N., & Yarin, V. I. (1962). Atlas of the airglow spectrum 3000–12400 Å. *Planetary and Space Science*, *9*(12), 883–915. https://doi.org/10.1016/0032-0633(62)90008-9

Krebsbach, M., & Preusse, P. (2007). Spectral analysis of gravity wave activity in SABER temperature data. *Geophysical Research Letters*, *34*, L03814. https://doi.org/10.1029/2006GL028040

Leena, P. P., Venkat Ratnam, M., Krishna Murthy, B. V., & Vijaya Bhaskara Rao, S. (2012). Detection of high frequency gravity waves using high resolution radiosonde observations. *Journal of Atmospheric and Solar - Terrestrial Physics*, *77*, 254–259. https://doi.org/10.1016/j.jastp.2012.01.003

Liu, A. Z., & Swenson, G. R. (2003). A modeling study of O_2 and OH airglow perturbations induced by atmospheric gravity waves. *Journal of Geophysical Research*, *108*(D4), 4148. https://doi.org/10.1029/2002JD002474

Lu, X., Liu, A. Z., Swenson, G. R., Li, T., Leblanc, T., & Mcdermid, I. S. (2009). Gravity wave propagation and dissipation from the stratosphere to the lower thermosphere. *Journal of Geophysical Research*, *114*, D11101. https://doi.org/10.1029/2008JD010112

Makhlouf, U. B., Picard, R. H., Winick, J. R., & Tuan, T. F. (1998). A model for the response of the atomic oxygen 557.7 nm and the OH Meinel airglow to atmospheric gravity waves in a realistic atmosphere. *Journal of Geophysical Research*, *103*(D6), 6261–6269. https://doi.org/10.1029/97JD03082

Marks, C. J., & Eckermann, S. D. (1995). A three-dimensional non-hydrostatic ray-tracing model for gravity waves: Formulation and preliminary results for the middle atmosphere. *Journal of the Atmospheric Sciences*, *52*(11), 1959–1984. https://doi.org/10.1175/1520-0469(1995)052%3C1959:ATDNRT%3E2.0.CO;2

Matsuda, T. S., Nakamura, T., Ejiri, M. K., Tsutsumi, M., & Shiokawa, K. (2014). New statistical analysis of the horizontal phase velocity distribution of gravity waves observed by airglow imaging. *Journal of Geophysical Research: Atmospheres*, *119*, 9707–9718. https://doi.org/10.1002/2014JD021543

Matsuda, T. S., Nakamura, T., Ejiri, M. K., Tsutsumi, M., Tomikawa, Y., Taylor, M. J., … Moffat-Griffin, T. (2017). Characteristics of mesospheric gravity waves over Antarctica observed by ANGWIN (Antarctic gravity wave instrument network) imagers using 3-D spectral analyses. *Journal of Geophysical Research: Atmospheres*, *122*, 8969–8981. https://doi.org/10.1002/2016JD026217

McLandress, C., Shepherd, T. G., Polavarapu, S., & Beagley, S. R. (2012). Is missing orographic gravity wave drag near 60°S the cause of the stratospheric zonal wind biases in chemistry–climate models? *Journal of the Atmospheric Sciences*, *69*(3), 802–818. https://doi.org/10.1175/JAS-D-11-0159.1

Mehta, D., Gerrard, A. J., Ebihara, Y., Weatherwax, A. T., & Lanzerotti, L. J. (2017). Short-period mesospheric gravity waves and their sources at the South Pole. *Atmospheric Chemistry and Physics*, *17*(2), 911–919. https://doi.org/10.5194/acp-17-911-2017

Moffat-Griffin, T., Hibbins, R. E., Jarvis, M. J., & Colwell, S. R. (2011). Seasonal variations of gravity wave activity in the lower stratosphere over an Antarctic Peninsula station. *Journal of Geophysical Research*, *116*, D14111. https://doi.org/10.1029/2010JD015349

Murphy, D. J., & Vincent, R. A. (2000). Amplitude enhancements in Antarctic MF radar echoes. *Journal of Geophysical Research*, *105*(D21), 26,683–26,693. https://doi.org/10.1029/2000JD900510

Nakamura, T., Higashikawa, A., Tsuda, T., & Matsushita, Y. (1999). Seasonal variations of gravity wave structures in OH airglow with a CCD imager at Shigaraki. *Earth, Planets and Space*, *51*(7-8), 897–906. https://doi.org/10.1186/BF03353248

Nappo, C. J. (2002). *An introduction to atmospheric gravity waves*. San Diego, CA: Academic Press.

Nielsen, K., Taylor, M. J., Hibbins, R. E., & Jarvis, M. J. (2009). Climatology of short-period mesospheric gravity waves over Halley, Antarctica (76°S, 27°W). *Journal of Atmospheric and Solar - Terrestrial Physics*, *71*(8-9), 991–1000. https://doi.org/10.1016/j.jastp.2009.04.005

Nielsen, K., Taylor, M. J., Hibbins, R. E., Jarvis, M. J., & Russell, J. M. (2012). On the nature of short-period mesospheric gravity wave propagation over Halley, Antarctica. *Journal of Geophysical Research*, *117*, D05124. https://doi.org/10.1029/2011JD016261

Nikoukar, R., Swenson, G. R., Liu, A. Z., & Kamalabadi, F. (2007). On the variability of mesospheric OH emission profiles. *Journal of Geophysical Research*, *112*, D19109. https://doi.org/10.1029/2007JD008601

Pautet, P. D., Stegman, J., Wrasse, C. M., Nielsen, K., Takahashi, H., Taylor, M. J., … Eckermann, S. D. (2011). Analysis of gravity waves structures visible in noctilucent cloud images. *Journal of Atmospheric and Solar - Terrestrial Physics*, *73*(14-15), 2082–2090. https://doi.org/10.1016/j.jastp.2010.06.001

Pramitha, M., Venkat Ratnam, M., Taori, A., Krishna Murthy, B. V., Pallamraju, D., & Vijaya Bhaskar Rao, S. (2015). Evidence for tropospheric wind shear excitation of high-phase-speed gravity waves reaching the mesosphere using the ray-tracing technique. *Atmospheric Chemistry and Physics*, *15*(5), 2709–2721. https://doi.org/10.5194/acp-15-2709-2015

Preusse, P., Eckermann, S. D., Ern, M., Oberheide, J., Picard, R. H., Roble, R. G., … Mlynczak, M. G. (2009). Global ray tracing simulations of the SABER gravity wave climatology. *Journal of Geophysical Research*, *114*, D08126. https://doi.org/10.1029/2008JD011214

Rapp, M., Gumbel, J., & Lübken, F.-J. (2001). Absolute density measurements in the middle atmosphere. *Annales de Geophysique*, *19*(5), 571–580. https://doi.org/10.5194/angeo-19-571-2001

Reeder, M. J., Adams, N., & Lane, T. P. (1999). Radiosonde observations of partially trapped lee waves over Tasmania, Australia. *Journal of Geophysical Research*, *104*(D14), 16,719–16,727. https://doi.org/10.1029/1999JD900038

Sato, K., Kohma, M., Tsutsumi, M., & Sato, T. (2017). Frequency spectra and vertical profiles of wind fluctuations in the summer Antarctic mesosphere revealed by MST radar observations. *Journal of Geophysical Research: Atmospheres*, *122*, 3–19. https://doi.org/10.1002/2016JD025834

Sato, K., Watanabe, S., Kawatani, Y., Tomikawa, Y., Miyazaki, K., & Takahashi, M. (2009). On the origins of mesospheric gravity waves. *Geophysical Research Letters*, *36*, L19801. https://doi.org/10.1029/2009GL039908

Stockwell, R. G., & Lowe, R. P. (2001a). Airglow imaging of gravity waves: 1. Results from a small network of OH nightglow scanning imagers. *Journal of Geophysical Research*, *106*(D15), 17,185–17,203. https://doi.org/10.1029/2001JD900035

Stockwell, R. G., & Lowe, R. P. (2001b). Airglow imaging of gravity waves 2. Critical layer filtering. *Journal of Geophysical Research*, *106*(D15), 17,205–17,220. https://doi.org/10.1029/2001JD900036

Suzuki, S., Shiokawa, K., Hosokawa, K., Nakamura, K., & Hocking, W. K. (2009). Statistical characteristics of polar cap mesospheric gravity waves observed by an all-sky airglow imager at Resolute Bay, Canada. *Journal of Geophysical Research*, *114*, A01311. https://doi.org/10.1029/2008JA013652

Swenson, G. R., & Gardner, C. S. (1998). Analytical models for the responses of the mesospheric OH* and Na layers to atmospheric gravity waves. *Journal of Geophysical Research*, *103*(D6), 6271–6294. https://doi.org/10.1029/97JD02985

Takahashi, T., Nozawa, S., Tsutsumi, M., Hall, C., Suzuki, S., Tsuda, T. T., … Fujii, R. (2014). A case study of gravity wave dissipation in the polar MLT region using sodium LIDAR and radar data. *Annales de Geophysique*, *32*(10), 1195–1205. https://doi.org/10.5194/angeo-32-1195-2014

Tateno, S., & Sato, K. (2008). A study of inertia-gravity waves in the middle stratosphere based on intensive radiosonde observations. *Journal of the Meteorological Society of Japan*, *86*(5), 719–732. https://doi.org/10.2151/jmsj.86.719

Taylor, M. J., Bishop, M. B., & Taylor, V. (1995). All-sky measurements of short period waves imaged in the OI(557.7 nm), Na(589.2 nm) and near infrared OH and O$_2$(0,1) nightglow emissions during the ALOHA-93 campaign. *Geophysical Research Letters*, *22*(20), 2833–2836. https://doi.org/10.1029/95GL02946

Taylor, M. J., Pautet, P. D., Medeiros, A. F., Buriti, R. A., Fechine, J., Fritts, D. C., … São Sabbas, F. T. (2009). Characteristics of mesospheric gravity waves near the magnetic equator, Brazil, during the SpreadFEx campaign. *Annales de Geophysique*, *27*(2), 461–472. https://doi.org/10.5194/angeo-27-461-2009

Tomikawa, Y. (2015). Gravity wave transmission diagram. *Annales de Geophysique*, *33*(12), 1479–1484. https://doi.org/10.5194/angeo-33-1479-2015

Tsuda, T. (2014). Characteristics of atmospheric gravity waves observed using the MU (middle and upper atmosphere) radar and GPS (Global Positioning System) radio occultation. *Proceedings of the Japan Academy. Series B*, *90*(1), 12–27. https://doi.org/10.2183/pjab.90.12

Vincent, R. A., Kovalam, S., Reid, I. M., & Younger, J. P. (2010). Gravity wave flux retrievals using meteor radars. *Geophysical Research Letters*, *37*, L14802. https://doi.org/10.1029/2010GL044086

Vincent, R. A., & Reid, I. M. (1983). HF Doppler measurements of mesospheric gravity wave momentum fluxes. *Journal of the Atmospheric Sciences*, *40*(5), 1321–1333. https://doi.org/10.1175/1520-0469(1983)040%3C1321:HDMOMG%3E2.0.CO;2

von Savigny, C., McDade, I. C., Eichmann, K. U., & Burrows, J. P. (2012). On the dependence of the OH* Meinel emission altitude on vibrational level: SCIAMACHY observations and model simulations. *Atmospheric Chemistry and Physics*, *12*(18), 8813–8828. https://doi.org/10.5194/acp-12-8813-2012

Walterscheid, R. L., Schubert, G., & Straus, J. M. (1987). A dynamical-chemical model of wave-driven fluctuations in the OH nightglow. *Journal of Geophysical Research*, *92*(A2), 1241–1254. https://doi.org/10.1029/JA092iA02p01241

Werner, R., Stebel, K., Hansen, G. H., Blum, U., Hoppe, U.-P., Gausa, M., & Fricke, K.-H. (2007). Application of wavelet transformation to determine wavelengths and phase velocities of gravity waves observed by lidar measurements. *Journal of Atmospheric and Solar - Terrestrial Physics*, *69*(17-18), 2249–2256. https://doi.org/10.1016/j.jastp.2007.05.013

Wrasse, C. M., Nakamura, T., Tsuda, T., Takahashi, H., Medeiros, A. F., Taylor, M. J., … Admiranto, A. G. (2006). Reverse ray tracing of the mesospheric gravity waves observed at 23°S (Brazil) and 7°S (Indonesia) in airglow imagers. *Journal of Atmospheric and Solar - Terrestrial Physics*, *68*(2), 163–181. https://doi.org/10.1016/j.jastp.2005.10.012

Wright, C. J., Hindley, N. P., Moss, A. C., & Mitchell, N. J. (2016). Multi-instrument gravity-wave measurements over Tierra del Fuego and the Drake Passage—Part 1: Potential energies and vertical wavelengths from AIRS, COSMIC, HIRDLS, MLS-Aura, SAAMER, SABER and radiosondes. *Atmospheric Measurement Techniques*, *9*(3), 877–908. https://doi.org/10.5194/amt-9-877-2016

Yang, G., Clemesha, B., Batista, P., & Simonich, D. (2008). Improvement in the technique to extract gravity wave parameters from lidar data. *Journal of Geophysical Research*, *113*, D19111. https://doi.org/10.1029/2007JD009454

Yue, J., Nakamura, T., She, C. Y., Weber, M., Lyons, W., & Li, T. (2010). Seasonal and local time variability of ripples from airglow imager observations in US and Japan. *Annales de Geophysique*, *28*(7), 1401–1408. https://doi.org/10.5194/angeo-28-1401-2010